

# Graphene–silicon phase modulators with gigahertz bandwidth

V. Sorianello<sup>1</sup>, M. Midrio<sup>2</sup>, G. Contestabile<sup>3</sup>, I. Asselberghs<sup>4</sup>, J. Van Campenhout<sup>4</sup>, C. Huyghebaert<sup>4</sup>, I. Goykhman<sup>5</sup>, A. K. Ott<sup>5</sup>, A. C. Ferrari<sup>5</sup> and M. Romagnoli<sup>1\*</sup>

**The modulator is a key component in optical communications. Several graphene-based amplitude modulators have been reported based on electro-absorption. However, graphene phase modulators (GPMs) are necessary for functions such as applying complex modulation formats or making switches or phased arrays. Here, we present a 10 Gb s<sup>-1</sup> GPM integrated in a Mach–Zehnder interferometer configuration. This is a compact device based on a graphene-insulator–silicon capacitor, with a phase-shifter length of 300 μm and extinction ratio of 35 dB. The GPM has a modulation efficiency of 0.28 V cm at 1,550 nm. It has 5 GHz electro-optical bandwidth and operates at 10 Gb s<sup>-1</sup> with 2 V peak-to-peak driving voltage in a push–pull configuration for binary transmission of a non-return-to-zero data stream over 50 km of single-mode fibre. This device is the key building block for graphene-based integrated photonics, enabling compact and energy-efficient hybrid graphene–silicon modulators for telecom, datacom and other applications.**

Optical communication systems for telecom and datacom implement high-order digital modulation schemes, such as amplitude or phase-shift keying, to enhance spectral efficiency and increase the data transmission capacity of telecommunication networks<sup>1</sup>. This is possible by encoding several bits of information in fewer symbols, resulting in reduced spectral bandwidth. Spectral narrowing is a key technique for optimizing data capacity in modern wavelength-division multiplexing (WDM) technology<sup>2</sup>, allowing higher data rates, improved spectral efficiency and robust tolerances to transmission impairments such as chromatic dispersion<sup>1</sup>.

To encode the information in complex formats, phase modulation is needed<sup>1</sup>. In integrated Si photonics, this is achieved by exploiting the free-carrier plasma dispersion effect<sup>3</sup>, whereby changes in electron and hole densities result in changes in the Si refractive index and absorption. In state-of-the-art Si modulators<sup>4–17</sup>, the complex index change can be driven by p–n junctions<sup>7–17</sup> or capacitors<sup>4–6</sup> built in Si waveguides, and applying a voltage to deplete or accumulate free carriers interacting with the propagating light. Either with a depleted p–n junction<sup>7–17</sup> under reverse bias or with a Si–insulator–Si (SIS) capacitor<sup>4–6</sup> operating in the accumulation regime, high-speed performances for simple and complex modulation formats have been demonstrated<sup>4–17</sup>. However, the Si free-carrier effect in the depleted p–n junction mode<sup>3</sup> typically requires millimetre-sized devices to accumulate a  $\pi$ -phase shift with 1–3 V driving voltage, even in the most efficient devices<sup>7</sup>. This tends to limit the modulation efficiency, defined as the product of the  $\pi$ -phase-shift voltage and length ( $V_{\pi}L$ )<sup>18</sup>, and increase the modulator energy consumption (energy per bit)<sup>19</sup>. The SIS capacitor modulators are more efficient, with  $V_{\pi}L$  between 0.2 and 0.7 V cm (refs. 4–6) depending on the thickness of the insulator. However, the top plate of these devices is made of poly-Si, which typically exhibits very low mobility and high free-carrier concentration<sup>20</sup>. The low mobility increases the series resistance and may limit the electro-optical

bandwidth<sup>5</sup>, while the high free carrier concentration induces high propagation losses because of the plasma absorption<sup>3</sup>. As a result, there is a trade-off between optical loss,  $V_{\pi}L$  and footprint, because higher free carrier densities with stronger plasma dispersion come at the expense of increased optical absorption<sup>18</sup> or limited dynamic range, that is, the maximum intensity or phase change for a given driving voltage<sup>18</sup>. Therefore, novel solutions with increased  $V_{\pi}L$ , reduced optical loss and miniaturized footprints are needed. Hybrid technologies relying on functional materials integrated on Si photonics waveguides are one option. InGaAsP membranes bonded on Si photonics waveguides were suggested for phase modulators<sup>21,22</sup>. These exploit the concept of the SIS capacitor modulator, with the advantage of replacing the lossy poly-Si top layer with an InGaAsP membrane with a larger free-carrier-induced change of the refractive index with respect to Si. Phase-shifters based on a 150 nm InGaAsP membrane on 5 nm Al<sub>2</sub>O<sub>3</sub> deposited on a Si waveguide showed a static  $V_{\pi}L$  of ~0.047 V cm at 1,550 nm (ref. 21), while an InGaAsP membrane on 10 nm SiO<sub>2</sub> on an n-doped Si waveguide core achieved 2 GHz bandwidth and  $V_{\pi}L=0.12$  V cm at the same wavelength<sup>22</sup>.

Graphene is appealing for photonics and optoelectronics because it offers a range of advantages compared to other materials, such as Si and other semiconductors<sup>23–26</sup>. In particular, graphene is ideally suited for integration into Si photonics<sup>27–33</sup> due to its large optical modulation<sup>27–31</sup>, broadband photodetection<sup>32,33</sup>, high-speed operation<sup>30,32</sup> and complementary metal oxide semiconductor (CMOS) compatibility<sup>27–33</sup>. The integration of graphene with Si photonics opens a new paradigm for developing compact, efficient and low-loss integrated phase modulators (PMs) that outperform state-of-the-art Si devices<sup>4–17</sup>. Due to its unique optoelectronic properties, optical losses in single-layer graphene (SLG) can be electrically suppressed due to Pauli blocking<sup>34–36</sup>. This results in modulation of the absorption, with a refractive index change much larger than the free carrier effect in Si<sup>31</sup>. Few demonstrations of a phase change

<sup>1</sup>Consorzio Nazionale per le Telecomunicazioni (CNIT), Photonic Networks and Technologies National Laboratory, Pisa, Italy. <sup>2</sup>Consorzio Nazionale per le Telecomunicazioni (CNIT), University of Udine, Udine, Italy. <sup>3</sup>Consorzio Nazionale per le Telecomunicazioni (CNIT), Scuola Superiore Sant'Anna, Pisa, Italy. <sup>4</sup>IMEC, Leuven, Belgium. <sup>5</sup>Cambridge Graphene Centre, Cambridge University, Cambridge, UK. \*e-mail: [marco.romagnoli@cnit.it](mailto:marco.romagnoli@cnit.it)

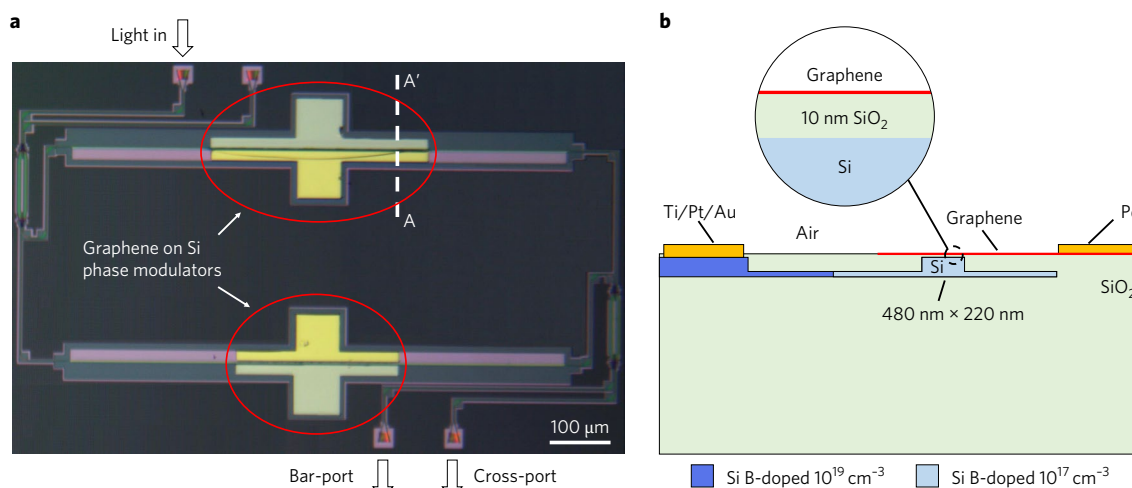


**Fig. 1 | Device.** **a**, Optical micrograph of the MZI modulator. The top arm has a 400  $\mu\text{m}$  SLG on Si, the bottom arm has a 300  $\mu\text{m}$  SLG on Si. **b**, Cross-section of the GPM through the dashed line A–A' of **a**. The ridge waveguide has a 480  $\times$  220 nm core with a 60-nm-thick lateral slab. The waveguide is B-doped at a concentration of  $\sim 1 \times 10^{17} \text{ cm}^{-3}$  (pale blue) in the core and in the slab up to 1  $\mu\text{m}$  from the core. Heavy B doping of  $\sim 1 \times 10^{19} \text{ cm}^{-3}$  (violet) is present in the contact region to improve the contact resistance on Si. The waveguide is embedded in a  $\text{SiO}_2$  cladding (light green) (2  $\mu\text{m}$  thick at the bottom and 10 nm thick on the top of the waveguide). SLG (red) is placed on top of the waveguide and extends  $\sim 0.5 \mu\text{m}$  beyond the waveguide core on the left side. Different metallizations (yellow) are used on Si and SLG: Ti(20 nm)/Pt(20 nm)/Au(30 nm) on Si, Pd(50 nm) on SLG.

induced by graphene integrated on Si have been reported<sup>37–39</sup>, but the effect is very weak and requires very high voltages (tens of volts). High-speed phase modulation has not yet been demonstrated. SLG-on-Si waveguides with an effective refractive index (that is, the ratio between the phase velocity of light in the waveguide and in vacuum) change larger than  $1 \times 10^{-3}$  have been demonstrated<sup>39</sup> (about ten times larger than in state-of-the-art Si p–n junction waveguides in depletion operation<sup>18</sup>). Consequently, in principle, SLG can provide a unique combination of a strong electro-refractive effect and optical transparency when operated in the Pauli blocking regime. The optical transparency of SLG is mainly limited by the quality of the transferred material<sup>31</sup>. To fully exploit the Pauli blocking regime, the transferred SLG should have a mobility  $> 10,000 \text{ cm}^2 \text{ V}^{-1} \text{ s}^{-1}$  at low carrier concentration (see Supplementary Section 1).

Here, we demonstrate a graphene PM (GPM) integrated in a Mach–Zehnder interferometer (MZI; Fig. 1a), in which the PM is realized in the form of a Si–insulator–SLG (SISLG) capacitor and the Si waveguide is used as a gating electrode to the SLG (Fig. 1b). By applying a bias to the capacitor, charge is accumulated on the SLG electrode, shifting its Fermi level and modifying its complex conductivity<sup>34–39</sup>. In this way, both the effective index and optical loss of the SLG-integrated Si waveguide can be tuned<sup>39</sup>. If the SLG is doped beyond the Pauli blocking condition (with Fermi level,  $E_F$ ,  $> 0.4 \text{ eV}$  at 1.55  $\mu\text{m}$ ), the device operates in the low-loss ‘transparency’ region, with the remaining losses due to the Si waveguide propagation losses without SLG (see Supplementary Section 2). In this regime, phase modulation is dominant with respect to amplitude changes<sup>31</sup>, with an enhanced modulation efficiency ( $V_\pi L < 0.26 \text{ V cm}$ )<sup>31</sup> compared to typical Si photonics modulators operating in the depletion mode ( $V_\pi L > 1 \text{ V cm}$ )<sup>18</sup>, and comparable to (or even better than) SIS capacitor modulators in accumulation mode ( $V_\pi L \approx 0.2–0.7 \text{ V cm}$ )<sup>4–6</sup>.

Our device was fabricated on a standard Si photonics platform using a Si-on-insulator (SOI) substrate (see Methods). The photonic structure consists of a balanced MZI, with 3 dB multimode interference (MMI) couplers<sup>40</sup> to split and combine the optical beam, and gratings<sup>41</sup> to couple light in and out of the device (Fig. 1a). The Si waveguide was designed to support a single transverse-electric (TE) in-plane polarized optical mode, and boron-doped to reduce

the Si resistance and achieve high-speed operation<sup>18</sup>. The SLG was grown by chemical vapour deposition (CVD) and then wet-transferred (see Methods) onto 10 nm planarized  $\text{SiO}_2$  top cladding (Fig. 1b). Different SLG lengths were used for the two MZI arms (300 and 400  $\mu\text{m}$ ) to introduce a bias phase difference in the balanced interferometer structure for characterization purposes. The quality and uniformity of SLG after device fabrication were characterized by Raman spectroscopy (see Methods). The spectra show a negligible D to G intensity ratio (Fig. 2), indicating that no significant degradation and/or defects have been introduced during the fabrication process<sup>42,43</sup>.

To test the electro-refractive effect, we first performed static characterizations by measuring the MZI output power as a function of bias voltage applied to the GPMs on both MZI arms (Fig. 3). A 1,550 nm laser source was coupled to the MZI input using a single-mode fibre (SMF), while the optical power at the MZI outputs, namely the bar- and cross-ports, was collected with a similar fibre and monitored by a power meter (see Methods). In our balanced MZI the cross-port was expected to be at a maximum when the phase difference between the two arms was zero, while the bar-port tended to be at zero power. We measured an output power difference of  $\sim 5 \text{ dB}$  between the two ports when no voltage was applied. We assigned this imbalance to the difference in absorption and phase accumulation between the two MZI arms caused by the different SLG lengths, doping and defects (Fig. 2). By applying a bias to the Si–SLG capacitors, we decreased the bar port power to zero, with an extinction ratio (ER, ratio between maximum and minimum of the transmission)  $> 35 \text{ dB}$  (Fig. 3b). This is ascribed to the phase change introduced in the two arms by electrical gating of SLGs. The 35 dB ER is due to the phase difference between the two arms approaching  $\pi$ , and this is evidence of the interferometric behaviour with a considerable electro-refractive effect. We obtained  $V_\pi \approx 7.25 \text{ V}$  on the 400  $\mu\text{m}$  Si–SLG capacitor, corresponding to  $V_\pi L \approx 0.28 \text{ V cm}$ , in agreement with the theoretical prediction (see Supplementary Section 2). This is a fivefold improvement compared to state-of-the-art p–n junction-based Si MZI modulators<sup>7</sup>. The proposed SLG-on-Si modulator exhibits lower  $V_\pi L$ , even with respect to the SIS capacitor modulator realized with same dielectric thickness and operating at the same wavelength, which

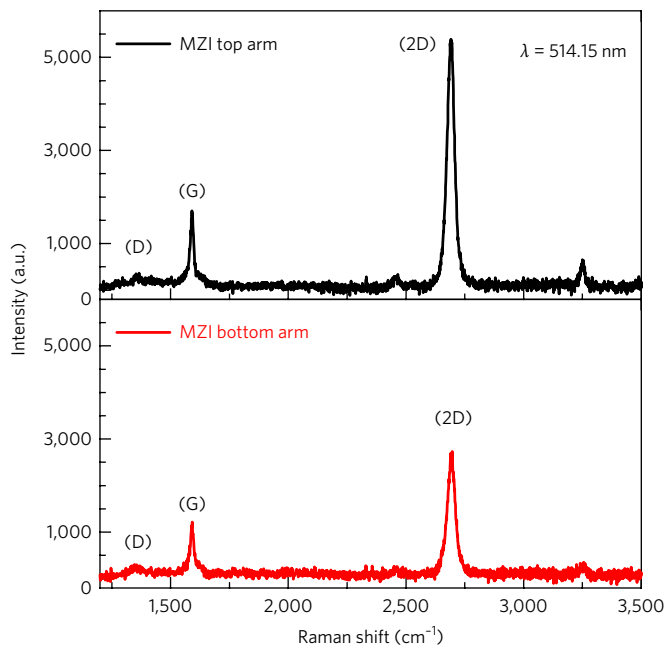


**Fig. 2 | Raman characterization.** Raman spectra of SLG at the top (black) and bottom (red) arms of the GPM, normalized to the Si Raman peak at  $521\text{ cm}^{-1}$ .

is expected to have  $V_{\pi}L = 0.4\text{ V cm}$  (refs <sup>4,5</sup>). The curves in Fig. 3 are normalized to the overall insertion losses. These are mainly due to the grating couplers, propagation losses in the doped Si waveguide not covered by the SLG, and propagation losses due to the SLG (see Supplementary Section 2). We note that the propagation loss of SLG is dependent on material quality. Here we have a mobility  $\sim 1,500\text{ cm}^2\text{ V}^{-1}\text{ s}^{-1}$  (see Methods), corresponding to an estimated insertion losses per unit length of  $\sim 236\text{ dB cm}^{-1}$  (see Supplementary Section 2). This gives a figure of merit (FOM), defined as the prod-

uct of the modulation efficiency  $V_{\pi}L$  (in unit of  $\text{V cm}$ ) and the insertion loss per unit length (in unit of  $\text{dB cm}^{-1}$ ) of  $\sim 62\text{ dB V}$ . This FOM can be reduced by improving the transfer process and encapsulating SLG within hexagonal boron nitride (hBN), allowing for mobility exceeding  $50,000\text{ cm}^2\text{ V}^{-1}\text{ s}^{-1}$  (ref. <sup>44</sup>), and giving a FOM  $\sim 14.5\text{ dB V}$  (see Supplementary Section 2), significantly better than a SIS capacitor modulator with the same dielectric thickness and operating at the same wavelength (FOM  $\sim 21.6\text{ dB V}$ ; ref. <sup>5</sup>). We also note that a PM based on high-mobility SLG and a double SLG structure<sup>31</sup> would give a FOM of  $\sim 1\text{ dB V}$ , outperforming the SISCAP<sup>4,5</sup> and competitive with hybrid III-V on Si modulators<sup>21,22</sup>. If the two SLGs are embedded in the core of the waveguide,  $V_{\pi}L$  could be further reduced to  $70\text{ mV cm}$  (ref. <sup>45</sup>).

To test the modulator electro-optical (EO) bandwidth and operation speed, we first characterized the frequency response using an electrical vector network analyser (VNA) (see Methods). We measured a 3 dB roll-off frequency of 5 GHz at 4 V (Fig. 4a). The bandwidth is limited by the RC time constant, primarily due to the Si-SLG capacitor and series resistances (see Methods). In our device, the metal-SLG contact resistance is the main factor limiting the radiofrequency (RF) bandwidth. The latter was estimated to be  $\sim 10\text{ k}\Omega\mu\text{m}$  by using a transfer length measurement (TLM) on test samples (see Methods). This can be improved by reducing the parasitic capacitance  $C_p$  and the series resistance  $R$ . Contact resistances down to  $100\Omega\mu\text{m}$  have been reported<sup>46</sup>. The Si series resistance  $R_{\text{si}}$  can be reduced by using thicker slabs, shortening the distance between the high-doping region and the waveguide core, or by introducing an intermediate-level doping. By optimizing the processes and the device geometry, the RF bandwidth could be raised to 30 GHz, leading to high-frequency operations comparable with state-of-the-art modulators<sup>4-17</sup>. This was demonstrated for electro-absorption modulators based on a SLG-insulator-SLG geometry<sup>30</sup>.

We now discuss the optical response when the MZI modulator is driven by a non-return-to-zero (NRZ) signal<sup>1</sup>. We measured the MZI NRZ eye diagram with the two GPMs biased at 3.5 V (that is, not in the full transparency region; at higher voltages the transmitted power drops below the sensitivity of the used photoreceiver)

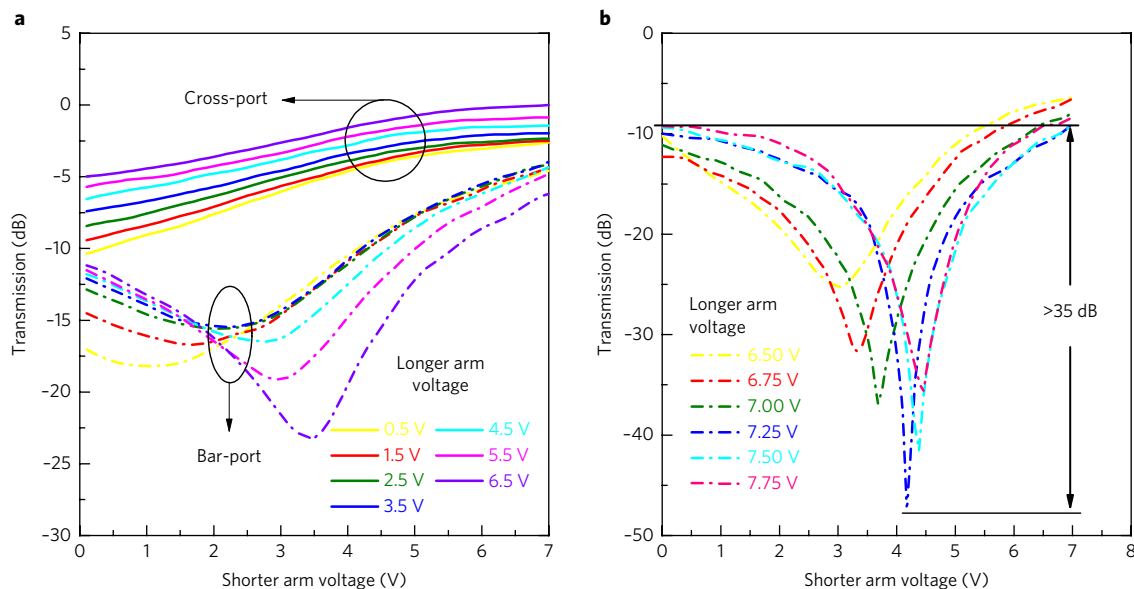


**Fig. 3 | Static electro-optical characterization.** **a**, Light output at  $1,550\text{ nm}$ , measured with the power meter at the bar-port (solid line) and cross-port (dashed lines), as a function of d.c. voltage applied to the shorter GPM (bottom arm in Fig. 1a). Different colours correspond to different d.c. voltages applied to the longer GPM (top arm in Fig. 1a). **b**, Extinction ratio at the bar port at  $1,550\text{ nm}$ . By applying  $4.1\text{ V}$  to the shorter GPM and  $7.25\text{ V}$  d.c. bias to the longer one, the phase difference between the two MZI arms approaches  $\pi$  and the extinction is maximized.

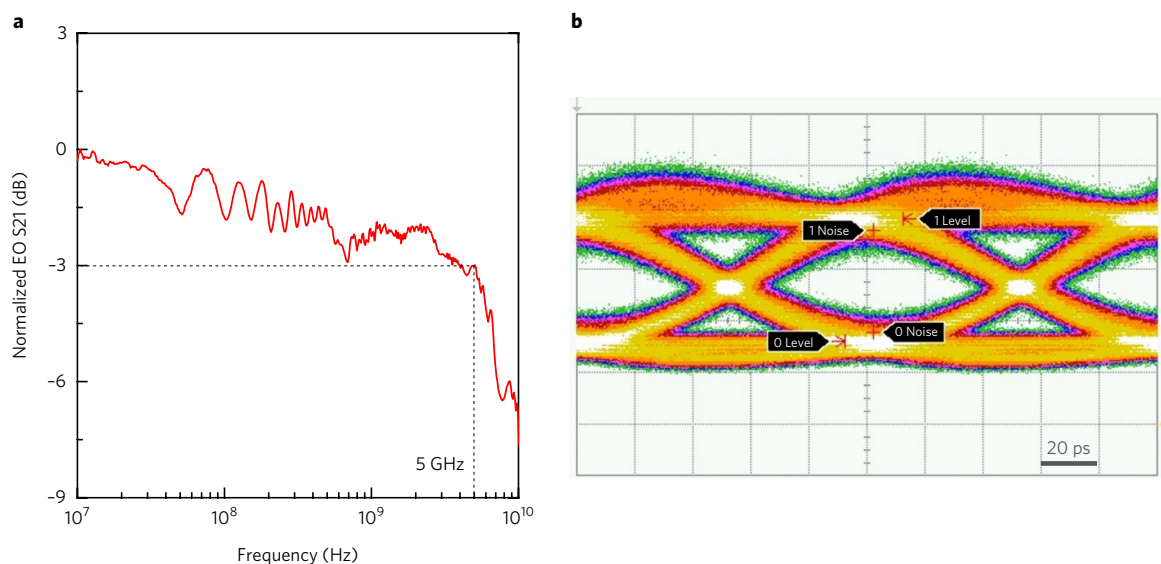


**Fig. 4 | Dynamic characterization.** **a**, Electro-optical S21 bandwidth of the GPM. The bandwidth is limited to 5 GHz by the large resistance of the metal SLG contact. **b**,  $2^{31}-1$  PRBS NRZ eye diagram at  $10 \text{ Gb s}^{-1}$  (timescale of 20 ps). The optical signal wavelength is 1,550 nm. The two GPMs are biased at 3.5 V d.c. and driven with a 2 V peak-to-peak RF signal. The eye diagram has 3.94 dB ER and 5.85 dB SNR.

(Fig. 3). Using SLG with better mobility would allow lower losses in the pure phase regime (see Supplementary Section 2). The MZI operates in a push-pull configuration with 2 V peak-to-peak and  $2^{31}-1$  pseudorandom binary sequence (PRBS)<sup>2</sup> signals. The peak-to-peak driving signal may be scaled down to 1 V by improving the material quality, phase-shifter geometry and length<sup>31</sup>. Figure 3b presents an open eye diagram at  $10 \text{ Gb s}^{-1}$  with  $\sim 4$  dB ER and  $\sim 6$  dB

signal-to-noise ratio. With a random bit stream, the individual GPM average energy consumption is given by<sup>19</sup>  $C(\Delta V)^2/4$ , where  $\Delta V$  is the dynamic voltage variation driven to the contacts to charge/discharge the GPM capacitance. In our device, we obtain  $\sim 1$  pJ per bit. The bias voltage does not contribute to the overall power consumption as negligible static leakage current flows in the Si-SLG capacitor<sup>19</sup>. The energy consumption could be reduced by using the SLG-insulator-SLG configuration, potentially allowing the driving voltage to be halved<sup>31</sup>.

We then carried out bit error rate (BER) measurements with the NRZ signal transmitted in a standard SMF over different distances (Fig. 5). We measured the BER as a function of the optical signal-to-noise ratio (OSNR) in back-to-back configuration and after propagation in SMF spools of different lengths from 10 to 50 km. We achieved error-free operation ( $\text{BER} < 1 \times 10^{-10}$ ) up to 30 km, but at longer propagation distances a BER floor appeared. However, considering that state-of-the-art systems currently employ a soft-decision forward-error correction (SD-FEC)<sup>47</sup>, with overhead in the 7–25% range and enabling a pre-FEC BER threshold up to  $3.4 \times 10^{-2}$  or even higher<sup>47</sup>, our modulator exhibits error-free operation up to 50 km.

In summary, we have demonstrated a graphene-silicon phase modulator operating in the gigahertz regime. We included it in a MZI device, demonstrating a static modulation depth of 35 dB and modulation efficiency of 0.28 V cm, outperforming state-of-the-art Si-based p-n junctions and comparable to SIS-capacitor-based Si modulators. The modulator operates at  $10 \text{ Gbit s}^{-1}$ , showing an open eye diagram and error-free transmission over 50 km SMF. These results pave the way to the realization of graphene modulators for a wide range of telecom applications where phase modulation is crucial.

## Methods

Methods, including statements of data availability and any associated accession codes and references, are available at <https://doi.org/10.1038/s41566-017-0071-6>.

Received: 20 January 2017; Accepted: 21 November 2017;  
Published online: 22 December 2017

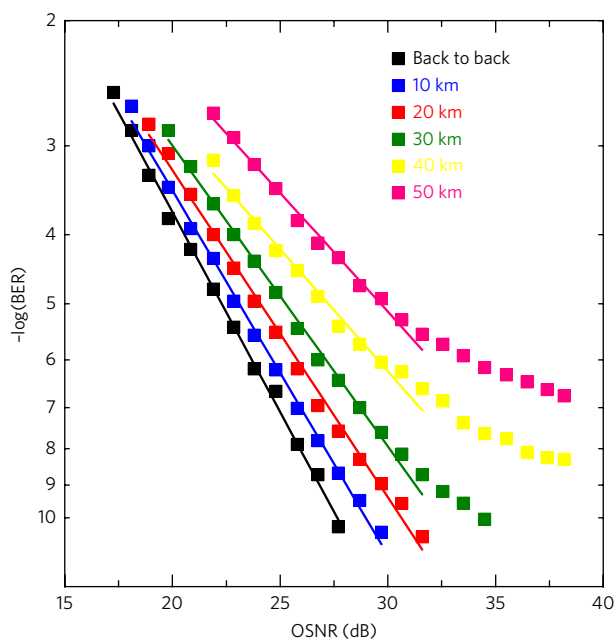


**Fig. 5 | Transmission measurements.** BER measurements of the  $2^{31}-1$  PRBS NRZ signal at  $10 \text{ Gb s}^{-1}$  (1,550 nm wavelength) as a function of OSNR in back-to-back configuration and after transmission over different standard SMF spool lengths. BER below  $1 \times 10^{-10}$  is achievable up to 30 km. Considering state-of-the-art systems employing SD-FEC, enabling a pre-FEC BER threshold in the range of  $1 \times 10^{-3}$ , the device demonstrates error-free operation for up to 50 km SMF transmission.

## References

- Seimetz, M. *High-Order Modulation for Optical Fiber Transmission* (Springer Verlag, Berlin, Heidelberg, 2009).
- Nakazawa, M., Kikuchi, K. & Miyazaki, T. *High Spectral Density Optical Communication Technologies* (Springer Verlag, Berlin, Heidelberg 2010).
- Soref, R. & Bennet, B. Electro-optical effects in silicon. *IEEE J. Quantum Electron.* **23**, 123–129 (1987).
- Xiaotie, W. *High Performance Optical Transmitter for Next Generation Supercomputing and Data Communication*. PhD thesis 820, Univ. Pennsylvania (2013); <http://repository.upenn.edu/edissertations/820>
- Abraham, A., Olivier, S., Marris-Morini, D. & Vivien, L. Evaluation of the performances of a silicon optical modulator based on a silicon-oxide-silicon capacitor. *Proc. 11th International Conference on Group IV Photonics* 3–4 (Paris, 2014).
- Webster, M. A. et al. Low-power MOS-capacitor based silicon photonic modulators and CMOS drivers. *Proc. 2015 Optical Fiber Communications Conference and Exhibition* 1–3 (Los Angeles, 2015).
- Xiong, C. et al. Monolithic 56 Gb/s silicon photonic pulse-amplitude modulation transmitter. *Optica* **3**, 1060–1065 (2016).
- Yu, H. et al. Performance tradeoff between lateral and interdigitated doping patterns for high speed carrier depletion based silicon modulators. *Opt. Express* **20**, 12926–12938 (2012).
- Wang, J. et al. Optimization and demonstration of a large-bandwidth carrier-depletion silicon optical modulator. *J. Lightw. Technol.* **31**, 4119–4125 (2013).
- Ding, J. et al. Ultra-low power carrier-depletion Mach–Zehnder silicon optical modulator. *Opt. Express* **20**, 7081–7087 (2012).
- Azadeh, S. et al. Advances in silicon photonics segmented electrode Mach–Zehnder modulators and peaking enhanced resonant devices. *Proc. SPIE* **9288**, 928817 (2014).
- Xiao, X. et al. High-speed, low-loss silicon Mach–Zehnder modulators with doping optimization. *Opt. Express* **21**, 4116–4125 (2013).
- Streshinsky, M. et al. Low power 50 Gb/s silicon traveling wave Mach–Zehnder modulator near 1300 nm. *Opt. Express* **21**, 30350–30357 (2013).
- Denoyer, G. et al. Hybrid silicon photonic circuits and transceiver for 50 Gb/s NRZ transmission over single-mode fiber. *J. Lightw. Technol.* **33**, 1247–1254 (2015).
- Reed, G. T. et al. Recent breakthroughs in carrier depletion based silicon optical modulators. *Nanophotonics* **3**, 229–245 (2013).
- Dong, P. et al. 50-Gb/s silicon quadrature phase-shift keying modulator. *Opt. Express* **20**, 21181–21186 (2012).
- Fresi, F. et al. Reconfigurable silicon photonics integrated 16-QAM modulator driven by binary electronics. *IEEE J. Sel. Top. Quantum Electron.* **22**, 6100210 (2016).
- Reed, G. T. *Silicon Photonics: The State of the Art* (Wiley, Chichester, 2008).
- Miller, D. A. B. Energy consumption in optical modulators for interconnects. *Opt. Express* **20**, A293–A308 (2012).
- Grundmann, M. *The Physics of Semiconductors: An Introduction Including Nanophysics and Applications*, 2nd edn (Springer, 2010).
- Han, J. H. et al. Efficient low-loss InGaAsP/Si hybrid MOS optical modulator. *Nat. Photon.* **11**, 486–490 (2017).
- Hiraki, T. et al. Heterogeneously integrated III–V/Si MOS capacitor Mach–Zehnder modulator. *Nat. Photon.* **11**, 482–485 (2017).
- Bonaccorso, F., Sun, Z., Hasan, T. & Ferrari, A. C. Graphene photonics and optoelectronics. *Nat. Photon.* **4**, 611–622 (2010).
- Kim, K. et al. A role for graphene in silicon-based semiconductor devices. *Nature* **479**, 338–344 (2011).
- Ferrari, A. C. et al. Science and technology roadmap for graphene, related two-dimensional crystals, and hybrid systems. *Nanoscale* **7**, 4598–4810 (2015).
- Castro Neto, A. H., Guinea, F., Peres, N. M. R., Novoselov, K. S. & Geim, A. K. The electronic properties of graphene. *Rev. Mod. Phys.* **81**, 109 (2009).
- Liu, M. et al. A graphene-based broadband optical modulator. *Nature* **474**, 64–67 (2011).
- Liu, M. et al. Double-layer graphene optical modulator. *Nano Lett.* **12**, 1482–1485 (2012).
- Hu, Y. et al. Broadband 10 Gb/s operation of graphene electro-absorption modulator on silicon. *Laser Photon. Rev.* **10**, 307–316 (2016).
- Phare, C. T. et al. Graphene electro-optic modulator with 30 GHz bandwidth. *Nat. Photon.* **9**, 511–514 (2015).
- Sorianello, V., Midrio, M. & Romagnoli, M. Design optimization of single and double layer graphene phase modulators in SOI. *Opt. Express* **23**, 6478–6490 (2015).
- Koppens, F. H. L. et al. Photodetectors based on graphene, other two-dimensional materials and hybrid systems. *Nat. Nanotech.* **9**, 780–793 (2014).
- Goykhman, I. et al. On-chip integrated, silicon-graphene plasmonic Schottky photodetector, with high responsivity and avalanche photogain. *Nano Lett.* **16**, 3005–3013 (2016).
- Wang, F. et al. Gate-variable optical transitions in graphene. *Science* **320**, 206–209 (2008).
- Falkovsky, L. A. Optical properties of graphene. *J. Phys.* **129**, 012004 (2008).
- Stauber, T. et al. Optical conductivity of graphene in the visible region of the spectrum. *Phys. Rev. B* **78**, 085432 (2008).
- Yu, S. L. et al. 2D materials for optical modulation: challenges and opportunities. *Adv. Mater.* **29**, 1606128 (2017).
- Moshin, M. et al. Experimental verification of electro-refractive phase modulation in graphene. *Sci. Rep.* **5**, 10967 (2015).
- Sorianello, V. et al. Complex effective index in graphene–silicon waveguides. *Opt. Express* **24**, 29984–29993 (2016).
- Soldano, L. B. & Pennings, E. C. M. Optical multimode interference devices based on self-imaging: principles and applications. *J. Lightw. Technol.* **13**, 615–627 (1995).
- Roelkens, G. et al. High efficiency silicon-on-insulator grating coupler based on a poly-silicon overlay. *Opt. Express* **14**, 11622–11630 (2006).
- Banszerus, L. et al. Ultrahigh-mobility graphene devices from chemical vapor deposition on reusable copper. *Sci. Adv.* **1**, e1500222 (2015).
- Cançado, L. G. et al. Quantifying defects in graphene via Raman spectroscopy at different excitation energies. *Nano Lett.* **11**, 3190–3196 (2011).
- Bruna, M. et al. Doping dependence of the Raman spectrum of defected graphene. *ACS Nano* **8**, 7432–7441 (2014).
- Midrio, M., Galli, P., Romagnoli, M., Kimerling, L. C. & Michel, J. Graphene-based optical phase modulation of waveguide transverse electric modes. *Photon. Res.* **2**, A34–A40 (2014).
- Leong, W. S. et al. Low-contact resistance graphene devices with nickel-etched-graphene contacts. *ACS Nano* **8**, 994–1001 (2014).
- Tzimpragos, G. et al. A survey on FEC codes for 100G and beyond optical networks. *IEEE Commun. Surv. Tut.* **18**, 209–221 (2016).

## Acknowledgements

The authors acknowledge funding from the European Union Graphene Flagship Project, ERC Grant Hetero2D and EPSRC grant nos. EP/509 K01711X/1, EP/K017144/1, EP/N010345/1, EP/M507799/5101 and EP/L016087/1. The authors also acknowledge Graphenea for the provision of CVD graphene samples.

## Author contributions

All authors conceived the phase modulator within the Graphene Flagship project. V.S., M.M., G.C. and M.R. carried out device design and testing. I.A., J.V.C. and C.H. fabricated the device. I.G., A.K.O. and A.C.F. performed material characterization.

## Competing interests

The authors declare no competing financial interests.

## Additional information

Supplementary information is available for this paper at <https://doi.org/10.1038/s41566-017-0071-6>.

Reprints and permissions information is available at [www.nature.com/reprints](http://www.nature.com/reprints).

Correspondence and requests for materials should be addressed to M.R.

**Publisher's note:** Springer Nature remains neutral with regard to jurisdictional claims in published maps and institutional affiliations.

## Methods

**Sample fabrication.** The Si photonic device was prepared on the IMEC iSiPP25G silicon on insulator (SOI) platform<sup>48</sup>. The MZI interferometer was based on Si ridge waveguides with a 60 nm slab and core cross-section of 480 nm × 220 nm. SLG was placed on the Si waveguide separated by a 10 nm spacer of high-quality thermal SiO<sub>2</sub>. Graphene was grown by CVD on copper foils, as described in ref.<sup>49</sup> and then transferred onto our Si samples following the procedure described in ref.<sup>50</sup>. Graphene patterning was carried out using a bilayer stack of PMMA/IX845, while etching was performed using conventional O<sub>2</sub> plasmas. The metal contacts on SLG and Si were processed separately in two consecutive steps. SLG was contacted with a single 50-nm-thick Pd layer, while the metal contact on Si consisted of a Ti/Pt/Au stack (20 nm/20 nm/30 nm) deposited on the Si surface after HF cleaning to remove the native SiO<sub>2</sub>. Contact resistance and mobility values were evaluated on different samples with equivalent processing. Typically values of 10 kΩ μm were extracted at the charge neutrality point using the TLM method, with a mobility of ~1,500 cm<sup>2</sup> V<sup>-1</sup> s<sup>-1</sup>.

**Raman characterization.** After device fabrication, the quality and uniformity of the SLG in both arms of the MZI were monitored by Raman spectroscopy using a Horiba LabRam Evolution Raman spectrometer with 514.5 nm laser and optical power below 0.1 mW to avoid damage. Raman spectra from the top and bottom arms (GPMs) of the MZI were normalized to the Si Raman peak at 521 cm<sup>-1</sup>. The 2D peak was a single Lorentzian with full-width at half-maximum (FWHM, 2D) of ~36 cm<sup>-1</sup> (~39 cm<sup>-1</sup>) at the top (bottom) arm of the MZI, a signature of SLG<sup>51</sup>. The spectra show negligible I(D)/I(G) of ~0.12 (~0.16), indicating that no significant degradation and/or defects were introduced during the fabrication process<sup>42,43</sup>. We estimated a defects density of ~2.3 × 10<sup>10</sup> cm<sup>-2</sup> and ~6.5 × 10<sup>10</sup> cm<sup>-2</sup> at the top and bottom GPMs, respectively<sup>42,43</sup>. Pos(G) is ~1,592 cm<sup>-1</sup> (~1,593 cm<sup>-1</sup>), with FWHM(G) of ~17 cm<sup>-1</sup> (~19 cm<sup>-1</sup>). The 2D peak position, Pos(2D) was ~2,691 cm<sup>-1</sup> (~2,693 cm<sup>-1</sup>), while the 2D to G peak intensity and area ratios I(2D)/I(G) and A(2D)/A(G) were 3.7 (2.6) and 8.2 (5.3), indicating a p doping <100 meV (~200 meV)<sup>52,53</sup> at the top (bottom) arm of the MZI. These correspond to carriers concentrations <1 × 10<sup>12</sup> cm<sup>-2</sup> (~2.3 × 10<sup>12</sup> cm<sup>-2</sup>)<sup>53</sup>.

**Electrical properties.** The overall capacitance  $C$  is the sum of the capacitance on top of the waveguide core ( $C_{ox} = \epsilon_0 \epsilon_{SiO_2} w_{wg} / t_{ox} \approx 1.6 \text{ fF } \mu\text{m}^{-1}$ , where  $\epsilon_0$  is the vacuum dielectric constant,  $\epsilon_{SiO_2}$  is the SiO<sub>2</sub> dielectric constant,  $w_{wg}$  is the waveguide core width and  $t_{ox}$  is the oxide thickness) and the parasitic capacitance  $C_p$  due to the SLG overlap on the Si slab ( $C_p = \epsilon_0 \epsilon_{SiO_2} w_{ol} / t_p \approx 0.2 \text{ fF } \mu\text{m}^{-1}$ , where  $w_{ol} \approx 1 \mu\text{m}$  is the overlap and  $t_p$  is the oxide thickness between the SLG and the Si slab).  $C_p$  depends on the alignment between the transferred SLG and the waveguide core, and it can contribute up to 20% of the overall  $C$ . The series resistance  $R$  has three different contributions: the Si resistance ( $R_{si}$ , estimated to be ~5 kΩ μm), the resistance of the SLG lead from the waveguide core to the metal contact ( $R_g$ , estimated to be <1 kΩ μm), and the metal-to-SLG contact resistance  $R_c$ .  $R_{si}$  was evaluated by numerical electrical simulations of the GPM cross-section, by using a commercial-grade device simulator that self-consistently solves the Poisson and drift-diffusion equations<sup>54</sup>. We used the Si doping and resistivity obtained from the IMEC iSiPP25G technology<sup>48</sup>. For the SLG we estimated a sheet resistance <400 Ω □<sup>-1</sup> when the SLG was gated beyond the Pauli blocking condition ( $E_F > 0.4 \text{ eV}$ ). This estimation was made with the following assumptions: at  $E_F > 0.4 \text{ eV}$  the carrier concentration exceeds  $1.3 \times 10^{13} \text{ cm}^{-2}$  ( $|n_s| = \pi^{-1} \times (E_F / (\hbar v_F))^2$ , where  $n_s$  is the carrier

concentration,  $\hbar$  is the reduced Planck constant and  $v_F$  is the Fermi velocity)<sup>54</sup>, and the mobility degradation from the ungated value is negligible<sup>55</sup>. As the SLG length from the waveguide core to the metal contact is 2.5 μm,  $R_g$  is easily estimated to be <400 Ω □<sup>-1</sup> × 2.5 μm = 1 kΩ μm.

**Experimental set-up.** Input/output optical coupling was obtained through cut SMFs with cleaved output surfaces. The input fibre was connected to the laser source with a fibre polarization controller to maximize the input coupled light. A tunable external cavity laser fixed at 1,550 nm was used. The output fibre was connected to a high-sensitivity power meter to measure the static characteristics in Fig. 3. Two ground signal (GS) high-frequency probes applied d.c. and RF signals to the two MZI GPMs. For small-signal RF bandwidth measurements, we used an electrical VNA. Its output was connected through a 50 Ω matched high-frequency cable to the GS probe contacting the GPM. We used a bias-tee to combine RF power and d.c. bias. We set a d.c. bias of 4 V and an RF power of -17 dBm. The light at the output of the MZI was modulated by the RF signal from the VNA and collected by a low-noise, high-frequency photodetector connected to the VNA input. The signals for the eye diagram and BER measurements were generated by a pattern generator (PG) and collected with a digital sampling oscilloscope (eye diagram) and a BER tester. The PG provided the 2<sup>31</sup>-1 PRBS at 10 Gb s<sup>-1</sup>. The signal and inverted signal were sent to the two GPMs through the RF cable and bias-tee. The optical input of the oscilloscope was used to collect light out of the MZI GPM and visualize the eye diagram of Fig. 4b. For BER evaluation, we used a high-frequency photoreceiver collecting the light at the output of the modulator and connected to the BER tester electrical input.

**Data availability.** The data that support the plots within this paper and other findings of this study are available from the corresponding author upon reasonable request.

## References

- Absil, P. et al. Imec iSiPP25G silicon photonics: a robust CMOS-based photonics technology platform. *Proc. SPIE* **9367**, 93670V (2015).
- Li, B. X. et al. Large-area synthesis of high-quality and uniform graphene films on copper foils. *Science* **324**, 1312–1314 (2009).
- Zurutuza, A., Centeno, A., Alonso, B. & Pesquera, A. Method of manufacturing a graphene monolayer on insulating substrates. US patent 9,023,220 B2 (2015).
- Ferrari, A. C. & Basko, D. M. Raman spectroscopy as a versatile tool for studying the properties of graphene. *Nat. Nanotech.* **8**, 235–246 (2013).
- Basko, D. M., Piscanec, S. & Ferrari, A. C. Electron–electron interactions and doping dependence of the two-phonon Raman intensity in graphene. *Phys. Rev. B* **80**, 165413 (2009).
- Das, A. et al. Monitoring dopants by Raman scattering in an electrochemically top-gated graphene transistor. *Nat. Nanotech.* **3**, 210–215 (2008).
- Lumerical Solutions, Inc; <http://www.lumerical.com/tcad-products/device/>
- Hirai, H. et al. Electron mobility calculation for graphene on substrates. *J. Appl. Phys.* **116**, 083703 (2014).